2010 IEEE International Conference on Robotics and Automation
Anchorage Convention District
May 3-8, 2010, Anchorage, Alaska, USA

Magnetic Field-based Sensing Method for Spherical Joint

Shaohui Foong, *Student Member, IEEE/ASME,* Kok-Meng Lee, *Fellow, IEEE/ASME* and Kun Bai

***Abstract*—This paper presents a sensing method that harnesses the capacity of modern sensors to measure vector fields. This approach directly maps distributed independent field measurements to the instantaneous orientation of a spherical joint embedded with low-cost permanent magnets. Unlike existing methods which require a priori and precise field models, this direct method engages an artificial neural network to associate a collection of measurements to joint orientation. The operation of both bipolar and unipolar single and multi-axis sensors were considered and evaluated experimentally.**

I. Introduction

Spherical joints allow for three degree-of-freedom (DOF) smooth manipulation in a single compact joint with no singularity except at boundaries of the workspace domain. It is heavily employed in a multitude of robotics and automation applications. When integrated with inexpensive rare-earth permanent magnets (PMs) and magnetic sensors, the joint orientation can be sensed unobtrusively. Compared to other sensing methods, magnetic fields have the advantage of passivity, permeability, invariance to environmental factors and free of 'line of sight' requirement, making it an appealing candidate for direct sensing.

The premise of non-contact sensing solutions, unlike single axis encoders which introduce friction, stiction, and inertia caused by constraining mechanisms, has motivated the adaptation of optical [1] and vision [2] sensors for measuring the 3-DOF orientation of a spherical body. Although high end sensors employing eddy current, capacitive and triangulation technologies are able to provide measurements with high precision, they only work with metallic surfaces, in clean environments and reflective exteriors respectively. Laser interferometers, which uses reflected laser light for measurements are too expensive and bulky. Inclinometers, accelerometers and other inertia/gyroscopic sensors offer an alternative means to measure the orientation and position through direct attachment to the moving body as it is done in aircrafts and Unmanned Aerial Vehicles (UAVs) [3]. However, the installation of these sensors not only introduce dynamical imbalance to the system and unless these sensors are powered autonomously and transmit measurements wirelessly, constrictive bridging connections are required.

Manuscript received September 15, 2009. This work was supported jointly by the Korea Institute of Machinery and Materials (KIMM) and Georgia Tech Foundation.

S. Foong, K.-M. Lee and K. Bai are with the Woodruff School of Mechanical Engineering at the Georgia Institute of Technology, Atlanta, GA 30332-0405 USA (e-mail: shao@gatech.edu; kokmeng.lee@me.gatech.edu; kbai@gatech.edu).

Harnessing vector fields for orientation/position sensing is not new as evident by Raab's et al. magnetic tracking system [4] introduced three decades ago. Despite major advancement in miniaturization and magnetic sensing technology where modern sensors possess small physical footprints and high sensitivity [5], the use of magnetic sensors for positional estimation remains under exploited. Although magnetic sensors offers many advantages, the main obstacle preventing widespread adoption is the complexity involved in determining the orientation/position with field measurements from the sensors. More recently, field models were used to localize the orientation and position of individual PMs. In [6], inverse computation of the PM's position is achieved using a nonlinear optimization algorithm to minimize the deviation between measured and modeled magnetic field (using a single dipole analytical model). This approach is relatively slow, high in complexity and requires a good initial guess of the parameters. A similar methodology is adapted in [7] for a decoupled multi-axis translational system. Lee and Son used the distributed multipole (DMP) model [8] to characterize the magnetic field of a single PM and design a magnetic field-based 2-DOF orientation sensor using methodically placed sensors [9]. For the above-mentioned techniques, the accuracy of the field model has a significant bearing on the resultant accuracy of the sensing system and not applicable in circumstances where the field model is unknown.

The remaining of this paper offers the following:

- We present a direct method that capitalizes on isolated and distributed magnetic field measurements for non-contact positional sensing. Approach undertaken here is not limited to magnetic fields but applicable to other vector fields and the relationship between measured field and position does need not be linear or explicitly known.
- This methodology relies on using a network of field based multi-axis sensors to detect variation in magnetic fields invoked by the moving PM field that can be inherent or supplementary to the system. An artificial neural network provides direct mapping between measured field and instantaneous position.
- Using a prototype spherical body, this technique is experimentally investigated using two types of multi-axis magnetic sensors: three-axis Hall-effect (bipolar) and two-axis GMR (unipolar) sensors and evaluated against an absolute inclinometer. Although single and two DOF approaches are shown, it is extendable to higher DOF positional sensing.

II. Direct Field-Based Sensing System

For a given dynamic system containing a moving vector field that is a function of its position/orientation, characterization of this inverse relationship between instantaneous field measurement and position is crucial for a field-based sensing system. Such fields can be artificially and intentionally added or inherent (natural) to the system. In a spherical joint/actuator [10], a system whose rotor possesses an inherent magnetic field from an assembly of PMs is presented to facilitate illustration. As shown in Fig. 1, these PMs are spaced equally on layers of circular planes such that their magnetization axes pass radially through ***O***. In addition, they are orientated such that their magnetization vector alternates between adjacent PMs (blue and red surfaces are north and south poles respectively).

A. Coordinate Systems and Sensor Placement

Fig. 1 defines the coordinate systems of the stator, rotor and orientation sensors, which are denoted as *XYZ* (reference), *xyz* (moving), and $X_pY_pZ_p$ (fixed local) respectively. The orientation of the *xyz* frame is described by a sequence of body-fixed rotations about *Z*, *y* and finally *z* axis by the corresponding angles of ψ, θ and ϕ respectively and this transformation can represented by

$$\begin{bmatrix} x & y & z \end{bmatrix}^T = \mathbf{\Gamma}(\mathbf{q}) \begin{bmatrix} X & Y & Z \end{bmatrix}^T \quad (1)$$

where $\mathbf{q}=[\psi,\theta,\phi]^T$ and $\mathbf{\Gamma}$ is the *zyz* Euler transformation matrix. ***O*** coincides with the center of the spherical bearing.

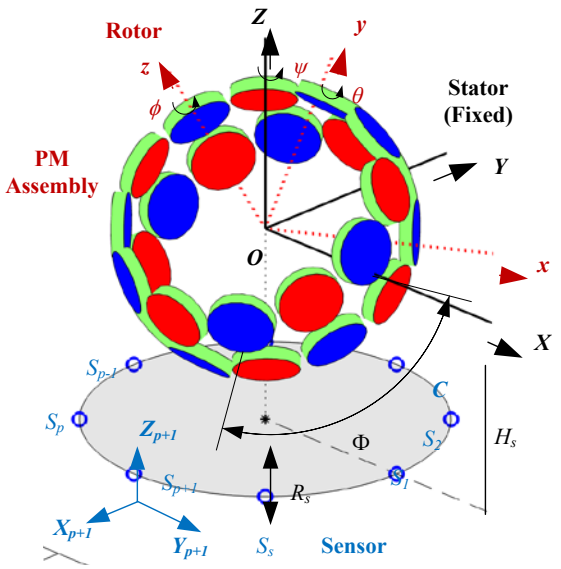

Fig. 1. Coordinate systems for rotor, stator and sensors

The stator contains *s* sensors (blue circles) spaced equally along a circular path **C** of radius R_s in a plane parallel to the *XY* plane. This sensor plane is displaced by $-H_s$ along the *Z*-axis. The p^{th} sensor position in the *XYZ* plane is

$$\mathbf{S_p} = R_s \begin{bmatrix} \cos((p-1)\psi_s) & \sin((p-1)\psi_s) & -H_s \end{bmatrix}^T \quad (2)$$

where p=1,2,…, s; and $\psi_s = 2\pi/s$ is the angular spacing between adjacent sensors. The sensors are orientated such that the sensing X_p and Y_p axis of each sensor are normal and tangential to **C**. Hence the coordinate transformation from the stator reference frame to the p^{th} sensor frame can be described by

$$\begin{bmatrix} X_p & Y_p & Z_p \end{bmatrix}^T = \mathbf{\Gamma}_S((p-1)\psi_s) \begin{bmatrix} X-R_s & Y & Z+H_s \end{bmatrix}^T \quad (3)$$

where $\mathbf{\Gamma}_S$ is the transformation matrix denoting rotation about *Z*-axis.

B. Field Mapping & Segmentation

In [11], a symmetric approach was used to classify the magnetic field mapping. Due to the offset positioning of the sensors from the *XY* plane, the field mapping loses some of its symmetric properties (notably about the *XY*-plane). In this paper, a more practical and general approach (assuming absence of field symmetry) is adopted and evaluated against the symmetric approach in [11]. It is noted that the field mapping for a rotor PM configuration is dependent on the location and orientation of the sensors.

Due to the alternating PM magnetization, spatial periodicity exists about the z-axis (a 2 × 2 PM configuration constitutes a single spatial period). If the axis of inclination is fixed or known (if ψ=0, the inclination axis will coincide with the stator *Y*-axis), a 2-D surface field map containing the magnetic flux density measurements of each axis (X_p,Y_p,Z_p) by each sensor at arbitrary inclination (θ) and spin (ϕ) can be constructed. As the range of rotor inclination is limited to $-\theta_{max} \le \theta \le \theta_{max}$ due to physical constraints, the domain of this surface map is

$$-\theta_{max} \le \theta \le \theta_{max}\ ,\ -\pi \le \phi \le \pi$$

If no symmetry is assumed or present, a typical surface map for the p^{th} sensor is shown in Fig. 2(a). Each sensing axis has its own dedicated surface map. For many devices and specifically in this spherical joint, the circular distribution of sensors and spatial periodicity Φ about the spin axis allows the surface map to be divided into $2\pi/\Phi$ segments as shown in Fig. 2(b). Within each segment, the localized map can be demarcated further into smaller sectors by considering only the *magnitude* of **B** and using the *direction* of **B** for sector selection and identification as discussed in [11]. Three different degrees of symmetry (in decreasing symmetry) are considered and visually illustrated in Fig. 2(b):

- *Type-A* symmetry: Assumes that the field contours residing in the sector defined by domain of $-\theta_{max} \le \theta \le \theta_{max}$ and $0 \le \phi' \le \Phi/4$ is unique and is related to the other 3 sectors through reflection and translation.
- *Type-B* symmetry: Assumes that the field contours are symmetric about the θ-axis or related by a translation of $\Phi/2$ in the ϕ'-axis. A type-B sector is defined by domain of $-\theta_{max} \le \theta \le \theta_{max}$ and $0 \le \phi' \le \Phi/2$.
- *Type-C* symmetry: No symmetry exists within a segment but like type-A and B, multiple segments are indistinguishable. The domain of a type-C sector coincides with the domain of a segment:

$-\theta_{\max} \le \theta \le \theta_{\max}$ and $-\Phi/2 \le \phi' \le \Phi/2$.

where ϕ' denotes the localized ϕ coordinate within a segment. A surface map exhibiting the most stringent Type-A symmetry will also posses both Type-B and C symmetry. But the converse does not hold.

While the preceding field mapping focused on the multiple sensing axis of a single sensor, it is possible to extend the concept of multi-axis mapping to establish multi-sensor field mapping in a network of sensors as depicted in Fig. 3. In multi-sensor field mapping, field measurements from a multiple sensors in a network can be utilized in a collaborative and complementary fashion. For example, a network of 3 single-axis sensors can produce 3 independent surface maps of the system just as a single three-axis sensor would generate. If segments are used, segments from different sensors can be combined to create an overall surface map (segment 1 from sensor 1, segment 2 from sensor 3 and so on). In addition, by combining both approaches, an integrated approach of multi-axis and multi-sensor field mapping is also feasible (An arbitrary segment can be constructed using the X_1-axis surface map of sensor 1 and Y_5-axis surface map of sensor 5).

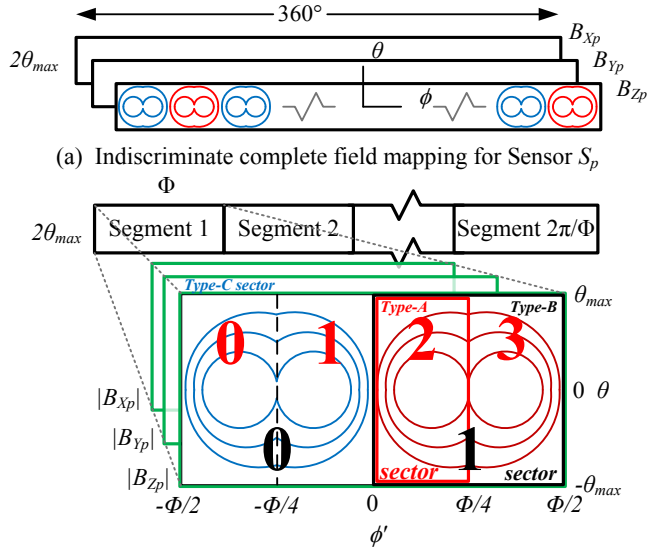

(a) Indiscriminate complete field mapping for Sensor S_p

(b) Sectorization and segmentation for type-A,B and C symmetry

Fig. 2. Different approaches in multi-axis field mapping

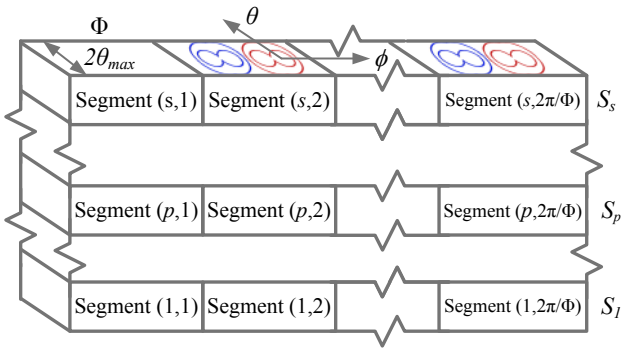

Fig. 3. Multi-sensor field mapping

C. *Artificial Neural Network Inverse Map*

Two-layer neural networks utilizing the Levenberg-Marquardt supervised back propagation algorithm are used to characterize the inverse mapping between the magnetic flux density measurements to the angular estimates of θ and ϕ. The entire surface map and sectionalized segments or sectors surface is discretized into a $M \times N$ grid, resulting to total of MN training-target sets; 80% of the sets will be used for training, 15% for validation and 5% for testing. For this application, the h hidden nodes neural network has i inputs (magnetic field measurements) and j outputs (target position) and can be mathematically represented in (4)

$$\left[\hat{\psi}_v \quad \hat{\theta}_v \quad \hat{\phi}_v\right]^T = \mathbf{NN}_h\left(\left\{B_{X1}(v), B_{Y1}(v), \cdots, B_{Ys}(v), B_{Zs}(v)\right\}\right) \quad (4)$$

where v is an integer representing the training set index ($1 \le v \le MN$), i=1,2,…,3s, j=1,2,3 and $\hat{\psi}_v, \hat{\theta}_v, \hat{\phi}_v$ are the angular estimates of the neural network. The mean squared error (MSE) is used to evaluate of the performance of a neural network and is expressed as:

$$\text{MSE} = \frac{1}{MN}\sum_{v=1}^{MN}\left[\left(\psi_v - \hat{\psi}_v\right)^2 + \left(\theta_v - \hat{\theta}_v\right)^2 + \left(\phi_v - \hat{\phi}_v\right)^2\right] \quad (5)$$

III. Experimental Investigation

Fig. 4 shows a prototype spherical joint/actuator, where the two-layered 24 PM assembly embedded in the rotor are N52 Neodymium PMs. Due to the arrangement of these PMs, the spatial periodicity is 60° which corresponds to 6 segments (from Fig. 2). Underneath the PMs is a separate assembly of electromagnets (EMs) on the stator, which when energized is used for actuation. As the location and input current of each EM is known and an iron-free structure, superposition of multiple magnetic fields is valid and allows active compensation of the EM field in the sensor measurements during operation.

In order to perform sensor calibration on the multi-DOF spherical actuator, the rotor is rigidly attached to a rotary track of radius R by means of a mechanical strut as shown in Fig. 5. The center of rotary track is positioned such that it coincides with the spherical bearing of the rotor. The arc length of the track contains measurement markings that allow correspondence between the curvature distance, w and inclination, θ. A dual-axis MEMS inclinometer (VTI Tech. SCA121T) provides an independent measurement as a direct comparison and an optical incremental encoder (Kübler T8.A02H) affixed onto the strut measures the spin motion of the rotor.

Table 1. Sensor specifications

	GMR	Hall	Inclinometer	Encoder
Type	Unipolar 2-axis (*YZ*)	Bipolar 3-axis (*XYZ*)	MEMS Dual-axis	Incremental quadrature
Range	1.4 mT	± 7.3 mT	± 30 °	unlimited
Sensitivity	320 mV/mT	280 mV/mT	70 mV/°	4000 counts/rev
Bandwidth(-3dB)	1 MHz	100 kHz	18 Hz	-
Price	$16	$24	$65 (chip)	-

Two types of magnetic sensors were used: a 3-Axis Hall-effect magnetic field sensor (Ametes MFS-3A) and a modified 2-axis Giant Magnetoresistance (GMR) (NVE Corp. AA003-02) which was prepared by attaching two single-axis GMR sensors. Table 1 summarizes the specifications of all sensors. The output of the magnetic sensors and inclinometer are transmitted in analog format as voltages digitally acquired using 16-bit (15-bit signed format) A/D converter banks. The quadrature outputs of the encoder are captured using a high-speed counter module. A gateway (Turck Inc. PG-GW-EN) attached to the A/D converter and counter module communicates with a HMI over Ethernet connection where the magnetic field, inclinometer and encoder measurements are displayed.

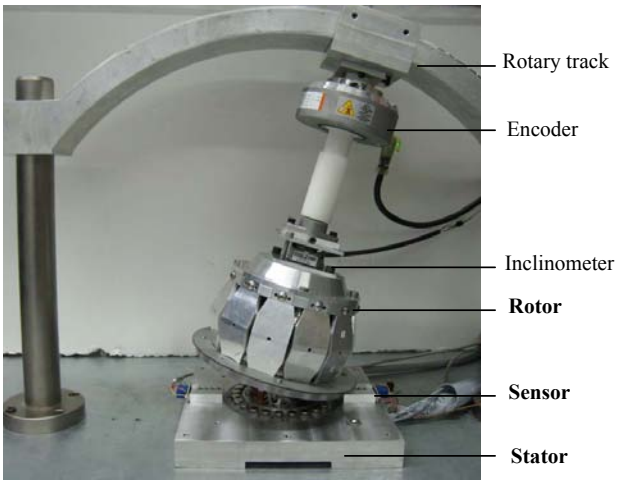

Fig. 4. Experimental Setup

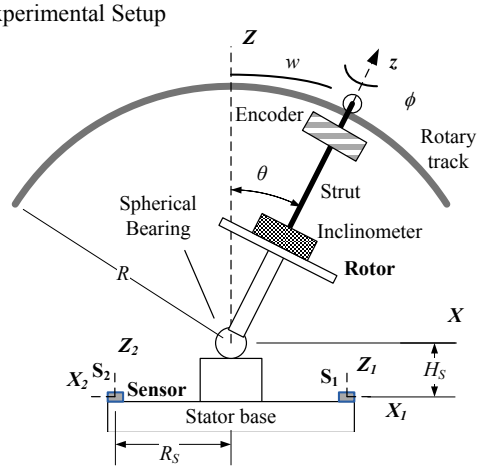

Fig. 5. Schematic of calibration setup

A. 1-DOF Inclination Characterization

For the experimental parameters listed in Table 2, the rotor was preset to known inclinations ($-22.5°<\theta<22.5°$) using the rotary track (at 5 mm increments measured on the track or 0.914° measured angularly) and the field measurements **B** of the magnetic sensors (GMR and Hall) were recorded while the spin of the rotor (rotation about the z-axis) is maintained at zero at all times ($\phi=0$). A typical set of field measurements is shown in Fig. 6 along with individual axis sensitivity which is defined as:

$$\text{Sensitivity} = \left| dB_\eta / d\theta \right| \quad (6)$$

where $\eta=X,Y$ or Z. As expected, due to symmetrical placement of sensors, the field measurements by S_1 and S_2 are mirrored about zero inclination. The sensitivity graphs suggest that the Y_p-axis field measurements are noticeably less responsive to inclination motion. As training ANN employs multiple axes for direct mapping, the aggregate sensitivity, expressed as,

$$\text{Aggregate sensitivity} = \left| dB_X / d\theta \right| + \left| dB_Y / d\theta \right| + \left| dB_Z / d\theta \right| \quad (7)$$

is used for evaluation. As sensor placement influences the overall sensing field sensitivity, a comparison illustrating the geometrical effect of R_s on aggregate sensitivity is shown in Fig. 7 for both Hall and GMR sensors. Reducing R_s generally increases the aggregate sensitivity as the sensor is closer to the PMs. But inherent physical limitation of sensors prevents them from being positioned too close to the PM due to field saturation as depicted by the dotted line. The optimum R_s for the Hall and GMR sensors found are 10.38 cm and 8.25 cm respectively.

Table 2. Parameters in experiment

Sensor:	s = 2, H_S = 3.04 cm
Setup:	R = 31.34 cm, θ_{max}=22.5°, Φ=60°

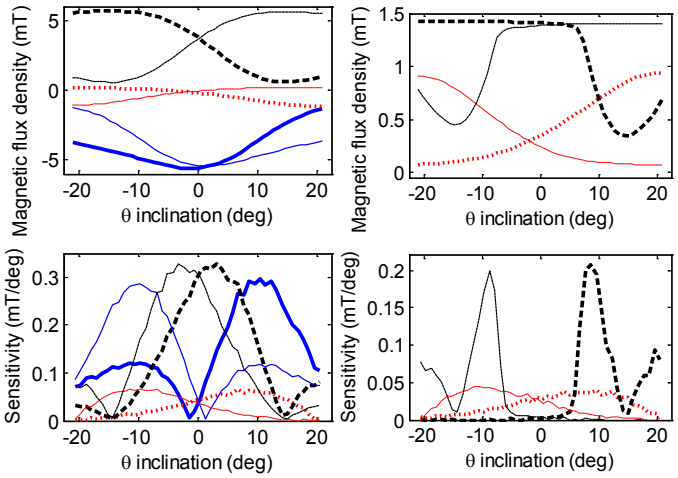

(a) Hall sensors (R_s=10.38 cm) (b) GMR sensors (R_s= 8.25 cm)

Fig. 6. Field measurements and sensitivity for magnetic sensors. B_X (solid-blue), B_Y (dotted-red), B_Z (dashed-black) and S_1(thick), S_2(thin).

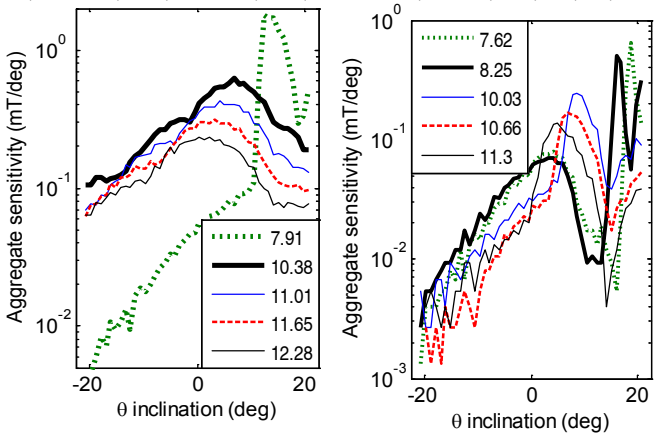

(a) Hall sensors (in S_1) (b) GMR sensors (in S_2)

Fig. 7. Aggregate sensitivity as a function of R_s (Units: cm)

It is desired to obtain the rotor inclination from isolated field measurements from the magnetic sensors. As the mapping between inclination and magnetic field measurements (of any single axis) is not bijective (encompassing one-to-one correspondence), it is not possible to derive a mathematical expression that describes the inclination of the rotor from measurements of a single axis from any sensor. Using various combinations of X_p, Y_p and Z_p measurements from two 3-axis Hall sensors and 2-axis GMR sensors to train an ANN with h=15, the MSE of the inclination estimate of each combinations are compiled in Table 3. Results in the table suggest that the MSE decreases with increasing number of sensing axis or sensors. As expected, single-axis trained ANN fared the worst due to non-bijectivity. However combining sensing measurements from multiple axes lowers the MSE significantly to order of 10^{-6} deg^2 (2-axes) and 10^{-8} deg^2 (3-axes) for the Hall sensors and 10^{-4} for GMR sensors. The results of multi-sensor trained ANNs follow the same trend as well; with the lowest MSE occurring when all sensing axes of multiple Hall and GMR sensors are used. The MSE of the inclinometer is spatially compared in Fig. 8 along with 3 Hall sensor trained ANNs: only Y_1-axis of S_1, X_1, Y_1 and Z-axis of S_1 and X_1, Y_1 and Z_1-axis of both S_1 and S_2. This direct field-based sensing mobilizing both unipolar and bipolar magnetic sensors outperforms the inclinometer in sensing accuracy as well as possessing a significantly higher bandwidth (ability to track rapid motion) at a lower cost as contrasted in Table 1.

Table 3. Comparison between combinations of multi-axis and multi-sensor field mapping (h=15)

Multi-axis		Multi-sensor/ Multi-axis		
3-axis bipolar Hall sensors (R_s = 10.38 cm)				
S_1	MSE (deg^2)	S_1	S_2	MSE (deg^2)
X	18.465	X	X	2.489×10^{-5}
Y	0.0101	Z	Z	3.942×10^{-5}
Z	1.688	X	Z	6.175×10^{-6}
XY	5.555×10^{-6}	XZ	X	1.330×10^{-7}
YZ	1.724×10^{-5}	XZ	Z	4.512×10^{-7}
XZ	1.842×10^{-6}	XZ	XZ	8.703×10^{-9}
XYZ	1.449×10^{-8}	XYZ	XYZ	2.512×10^{-10}
2-axis unipolar GMR sensors (R_s = 8.25 cm)				
Y	0.0164	Y	Y	0.0105
Z	49.387	Z	Z	0.2756
YZ	3.488×10^{-4}	YZ	Y	1.387×10^{-7}
		YZ	YZ	1.216×10^{-8}
		Inclinometer		0.0143

B. 2-DOF Concurrent Characterization

A 2-D surface map depicting the field measurements at arbitrary inclination and spin of the rotor is achieved using both the rotary track and encoder. Similar to the 1-DOF characterization, the rotor was preset to known inclinations (47 discrete points) using the rotary track and the field measurements **B** of the magnetic Hall sensors were recorded as the spin of the rotor is manually rotated at 0.36° increments (1000 data points per inclination set point). A complete surface map (2-D image with 47×1000 pixels) for the Y_p-axis measurement is shown in Fig. 9 along with the three sector types: Type A (47×42 pixels), Type B (47×84 pixels) and Type C (47×167 pixels). 6 distinct segments can be easily detected in Fig. 9(a) and are numbered using roman numerals. While sectors in B_Y can be classified up to Type-A symmetry, the sectors in B_X and B_Z can only be categorized up to Type-B symmetry due to the offset placement (H_s) of the sensors.

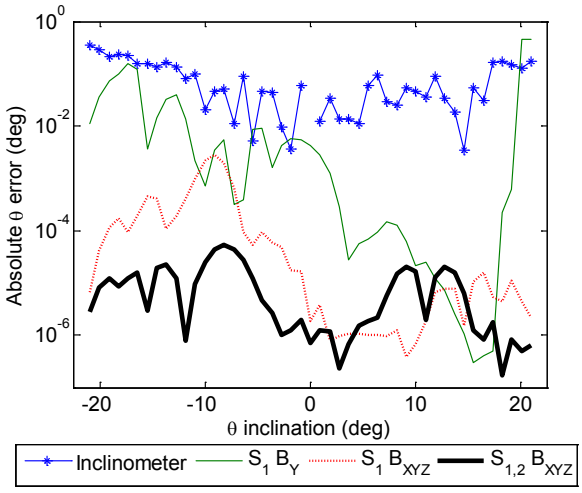

Fig. 8. Absolute error comparison between inclinometer and trained ANNs.

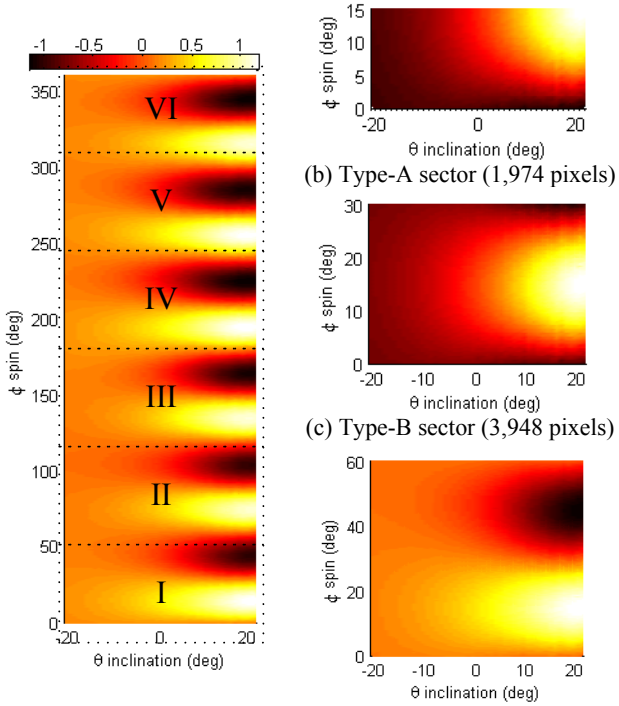

(a) Global surface map (b) Type-A sector (1,974 pixels) (c) Type-B sector (3,948 pixels) (d) Type-C sector (7,849 pixels)

Fig. 9. Different surface maps for B_Y of S_1. (R_s=10.38 cm) Units: milliTesla

Using segment I as the primary training segment, the Type-B and C sectors for each sensing axis of both sensors can be used to train ANNs with h=50. The spatial distribution of the absolute estimation error from the trained ANN using all 6 axes from both sensors and presuming Type-B symmetry is shown in Fig. 10. Assuming the

respective symmetry holds within segment *I* and replicated in other segments, the MSE resulting from operating an ANN trained for segment *I* using data in each of the remaining 5 segments are computed in Table 4. The MSE obtained from a trained ANN that assumes no spatial periodicity or symmetry in field measurements is provided for comparison. Also included in the table are the corresponding MSE if only B_X and B_Z (from each sensor) were utilized during training.

The results clearly suggest that ignoring the inherent symmetry of the system results in high MSE of the trained ANN. Assuming Type-B and C symmetry reduces the overall MSE significantly in the sector/segment which was used for training while recycling the trained ANN for operation in other segments is some orders of magnitude higher due to variation in strength of magnetic fields in PMs. However these errors are still much lower than an indiscriminate map of the entire global surface.

To achieve the lowest overall MSE, each segment (Type-C) should be individually trained using independent ANNs (in this case, 6 distinct ANNs), resulting in a more spatially consistent MSE as shown in the right most column of Table 4. Hence during operation all six ANNs will be used separately depending on the estimated spin position of the rotor obtained from a filter/predictor.

Table 4. Effects of symmetry on MSE (Segment *I*: primary)

	MSE (deg^2)						
h=50	$S_{1,2}B_{X,Z}$			$S_{1,2}B_{X,Y,Z}$			
Symmetry	Type-B	Type-C	None	Type-B	Type-C	None	Ind. C
Sector	0.00525	0.954		0.00262	0.00826		
Seg. *I*	1.38			9.75			**0.0082**
Seg. *II*	2.32	702		11.3	36.8		**0.0096**
Seg. *III*	17.65	1140		15.0	51.1		**0.0113**
Seg. *IV*	5.41	1470		13.4	3.78		**0.0091**
Seg. *V*	3.95	865		7.64	39.2		**0.0073**
Seg. *VI*	9.98	3190		19.3	96.2		**0.0101**
Global	6.78	1230	2340	12.7	37.8	498	**0.0092**

IV. Conclusion

We have presented a direct vector field-based sensing method to measure the position/orientation of a dynamic system with measurements from a network of multi-axis sensors. This method requires neither a prior accurate model of the field nor linearity with respect to sensing position but employs a neural network to directly map isolated field measurements to position. Using a spherical body with an embedded magnetic field as a platform for illustration and experimental analysis, the sensing error associated with using an ANN trained from multi-axis measurements from multiple unipolar and bipolar magnetic sensors was investigated. Although multi-axis sensors were used, this technique can be adapted for applications where only single-axis sensors are available using multi-sensor field mapping. When compared to an absolute inclinometer, this direct field-based sensing system possesses better accuracy, higher bandwidth, low cost and is extendable to multi-DOF sensing.

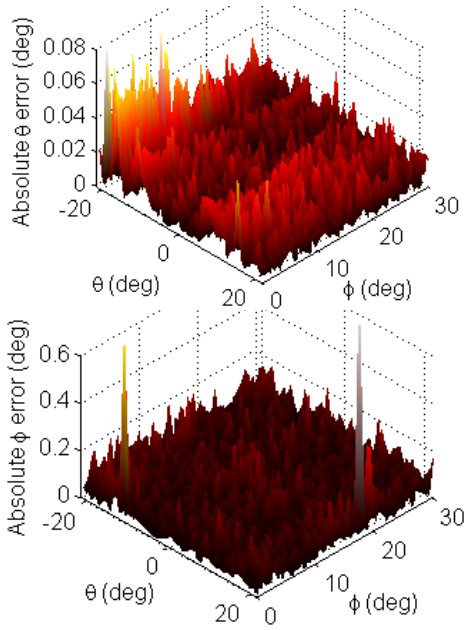

Fig. 10. Absolute spatial error distribution for inclination (top) and spin (bottom) estimates of segment *I* (*h*=75,Type-B sector)

Acknowledgment

This work was supported jointly by the Korea Institute of Machinery and Materials (KIMM) and Georgia Tech Foundation.

References

[1] K.-M. Lee and D. Zhou, "A Real-Time Optical Sensor for Simultaneous Measurement of Three-DOF Motions," *IEEE/ASME Transactions on Mechatronics*, vol. 9, no. 3, pp. 499-507, Sep 2004.

[2] H. Garner, M. Klement, and K.-M. Lee, "Design and Analysis of an Absolute Non-Contact Orientation Sensor for Wrist Motion Control," *Proceedings of IEEE/ASME International Conference on Advanced Intelligent Mechatronics*, Jul 2001.

[3] H. H. Djambazian, C. Nerguizian, V. Nerguizian, and M. Saad, "3D Inclinometer and MEMS Acceleration Sensors," *IEEE ISIE*, Jul 2006.

[4] F. H. Raab, E. B. Blood, T. O. Steiner, and H. R. Jones, " Magnetic Position and Orientation Tracking System," *IEEE Transactions on Aerospace and Electronic Systems*, vol. AES-15, no. 5, pp. 709-718, Sep 1979.

[5] J. Lenz and A. S. Edelstein, "Magnetic Sensors and Their Applications," *IEEE Sensors Journal*, vol. 6, no.3, pp. 631-649, Jun 2006.

[6] C. Hu, M. Q.-H. Meng, M. Mandal, "A Linear Algorithm for Tracing Magnet Position and Orientation by Using Three-Axis Magnetic Sensors," *IEEE Transactions on Magnetics*, vol. 43, no.12, pp. 4096-4101, Dec 2007.

[7] M.-C. Tsai, and C.-H. Yang, "A Flux-Density-Based Electromagnetic Servo System for Real-Time Magnetic Servoing/Tracking," *IEEE/ASME Transactions on Mechatronics*, vol. 13, no. 2, pp. 249-256, Apr 2008.

[8] K.-M. Lee and H. Son, "Distributed Multipole Model for Design of Permanent-Magnet-based Actuators," *IEEE Transactions on Magnetics*, vol. 43, no. 10, pp. 3904–3913, Oct. 2007.

[9] H. Son and K.-M. Lee, "Distributed Multipole Models for Design and Control of PM Actuators and Sensors," *IEEE/ASME Transactions on Mechatronics*, vol. 13, no 2, pp. 228-238, Apr 2008.

[10] K.-M. Lee, K. Bai, J. Lim, "Dipole Models for Forward/Inverse Torque Computation of Spherical Motor," *IEEE/ASME Transactions on Mechatronics*, vol 14, no. 1, pp 46-54, Feb 2009.

[11] S. Foong and K-M. Lee," Magnetic Field-Based Multi-DOF Orientation Sensor for PM-Based Spherical Actuators," *IEEE/ASME Advanced Intelligent Mechatronics*, pp. 481- 486, Jul 2009.